THE EUROPEAN
PHYSICAL JOURNAL A

Regular Article – Theoretical Physics

Neutrino diffusion in the pasta phase matter within the Thomas-Fermi approach

U.J. Furtado[1,2,a], S.S. Avancini[1,2,b], J.R. Marinelli[1,c], W. Martarello[1,d], and C. Providência[2,e]

[1] Departamento de Física, CFM, Universidade Federal de Santa Catarina, Florianópolis - SC, CP. 476, CEP 88040-900, Brazil
[2] CFisUC, Department of Physics, University of Coimbra, P3004-516 Coimbra, Portugal

Abstract. The behaviour and properties of neutrinos in non-uniform nuclear matter, surrounded by electrons and other neutrinos are studied in the protoneutron star early stage characterized by trapped neutrinos. The nuclear matter itself is modelled by a relativistic mean-field approach, and models with both constant couplings and density-dependent couplings are considered. The so-called nuclear pasta phases at sub-saturation densities, described using the Thomas-Fermi approximation and solved in a Wigner-Seitz cell, are included in the calculation. We obtain the neutrino total cross section and mean free path, taking into account scattering and absorption processes and we compare the final results obtained with different parametrizations. The solution for this problem is important for the understanding of neutrino diffusion in a newly born neutron star after a supernovae explosion. It is shown that the pasta phase will increase the neutrino mean free path by as much as an order of magnitude, therefore contributing for shorter emission time-scales.

1 Introduction

Neutrinos are elementary particles that interact with other particles only through the weak force and gravity, and, therefore, neutrino scattering by matter is very unlikely. On the other hand, this pure weak-force scattering can reveal some aspects of the structure of matter that other stronger interactions cannot. Also, this feature represents an advantage in the sense that neutrinos carry information from the target along great distances, as is the case of neutrinos produced in the interior of stars that reach earth detectors. For these reasons, the study of neutrino interaction with matter is at the same time very fruitful but very challenging. In what refers to the scattering of neutrinos by hadronic matter, despite the experimental and theoretical problems, some important progress has been made, examples are the Karmen collaboration [1] and Los Alamos results [2]. More recently, long-baseline experiments are under way, like MiniBoone, NOvA and other similar accelerator experiments [3,4]. Although the main purpose is to obtain further information on the Standard Model and on neutrino oscillations, a precise knowledge of the neutrino-hadron interaction as well as the hadronic structure of the targets [5] is necessary.

Another important source of information comes from the physics of core-collapse supernovae and neutron star evolution. The important ingredient in this case is the propagation of neutrinos in such a medium, which contains not only baryons but also leptons. In particular, for baryonic densities below the nuclear saturation value, structures known as pasta phases [6] are expected. These clusters may have exotic shapes and are embedded in a neutron and electron background gas. Actually, a delicate competition between Coulomb and surface energies determines the most favourable final inhomogeneous structure. The presence of such structures has a non-negligible role in the neutrino diffusion which is a key ingredient for the modelling and simulation of core-collapse supernovae mechanisms [7–9].

The models for core-collapse supernovae have evolved in the last decades, allowing presently, under certain conditions, for a neutrino-driven explosion. The mechanisms that drive the evolutionary stages of massive stars [10] from collapse to explosion and, later, formation of a protoneutron star (PNS) are not yet completely understood. However, a huge progress in this area has been done due to the improvements in the treatment of neutrino interactions and transport in a dense medium [11–13] and, simultaneously, due to a better knowledge of the nuclear equation of state (EOS). Of course, these inputs are crucial for the simulations to succeed in producing an explosion and quantitatively describe the nucleosynthesis. Under the current view, just after the supernova explo-

[a] e-mail: `ujfurtado@gmail.com`
[b] e-mail: `sidney@fsc.ufsc.br`
[c] e-mail: `ricardo.marinelli@ufsc.br`
[d] e-mail: `williams85@gmail.com`
[e] e-mail: `cp@fis.uc.pt`

sion, a PNS is formed at its center made out of dense, hot, quite proton-rich and neutrino-opaque matter, which by the combined process of deleptonization and energy loss, becomes a cold, neutrino-transparent and neutron-rich compact star. In the early stages of a PNS the neutrinos are trapped, since their mean free path is considerably smaller than the neutron star radius. In this stage, the neutrinos are essentially degenerate. However, in a few seconds the trapped neutrinos diffuse out to the neutrinosphere, heating the star while decreasing the net lepton and proton fractions.

In this work we are particularly interested in understanding whether, in this stage of trapped neutrinos, the non-homogeneous stellar matter existing in a density range 0.1–0.7 ρ_0, where ρ_0 is the normal nuclear matter density (2.5×10^{14} g/cm^3), affects the interaction of neutrinos with stellar matter, and, consequently, their mean free path.

The study of the effect of the pasta phase on the PNS evolution, in particular on the neutrino diffusion, has been also considered previously [8,9]. In the first case, a quantum molecular dynamics simulation based on a simple pure phenomenological interaction, which takes into account only neutral-current neutrino-target collisions, was used to obtain the cross sections. In the second case [9], a more realistic interaction was used to calculate the pasta structure but within a very simplified approach to determine the cross section. Even so, in this last case, an important difference, compared to homogeneous matter, was found in the total neutrino diffusion coefficients when the pasta phase is considered. Also, recent simulations [14], have shown that temperatures and densities close to the edge of the PNS could be compatible with the expected conditions for the pasta phase formation, a few seconds after bounce.

In [13], the authors have emphasized the importance of treating the neutrino-matter interaction consistently with the EOS. It was also shown that high-energy neutrinos, compatible with the energy of neutrinos considered in this work, are produced at an early stage of the PNS evolution. In ref. [15], the authors have considered the interaction of trapped neutrinos with beta-equilibrated homogeneous matter having a fixed electron lepton fraction. Their results are appropriate for the early stage of the PNS evolution and the neutrinos are taken at the Fermi energy ($E_\nu = \mu_\nu$) for several temperatures and special attention is given for supra nuclear densities. In our work, we also consider matter in beta-equilibrium with a fixed electron lepton fraction. However, our focus is on the neutrino interaction with non-homogeneous matter (pasta phase) just below saturation density which has not been studied in the literature in the present context. We choose the electron lepton fraction $Y_l = 0.2$, a value that was also taken in ref. [9] for the pasta phase investigation and which is consistent with recent PNS simulations [16].

Recently in [16], it has been shown that the properties of the EOS will affect the supernovae evolution, and, in particular, it was shown that the behaviour of the symmetry energy, which defines the electron fraction, will have some impact on the early stages of the evolution. Therefore, in the present work, which refers precisely to the early stages, we will discuss the effect of the density dependence of the symmetry energy on the neutrino mean free path. This is a quantity that is constrained by nuclear experiments [17].

One way to obtain the pasta phase is to solve the problem considering charge neutral Wigner-Seitz cells of appropriate geometries containing neutrons, protons and electrons within a variational approach, using both relativistic and non-relativistic mean-field calculations. Most of the recent applications in this case have used the Thomas-Fermi approximation [6,18,19], but Hartree-Fock calculations [20] and three-dimensional Thomas-Fermi calculations [21] are also found in the literature, all within the Wigner-Seitz approximation. Recently, it was shown in [21,22] that performing a pasta calculation taking a large enough cell to include several units of the pasta structures, distributions of matter different from the usual ones considered within the Wigner-Seitz (WS) approximation could be energetically favoured in some density ranges. Another approach to this problem, that also goes beyond the WS approximation, is based on the so-called quantum molecular dynamics [23–28] approach.

Here we follow the Thomas-Fermi results as described in [29] in order to generate the pasta phase structure, starting from a field theoretical approach. The self-consistent calculation is performed considering matter in β-equilibrium, where only protons, neutrons, electrons and neutrinos are present. The total neutrino cross section for each kind of particle is calculated, as a function of the density, taking into account the corresponding geometry for the considered density, *i.e.*, droplet, rod, slab, tube or bubble. The neutrino mean free path (NMFP) energy and temperature dependence are also discussed.

The neutrino cross section calculation includes the effects of strong interaction, and accounts for in-medium mass and energy shifts and degeneracy effects, based on the formalism previously developed for homogeneous nuclear matter [15], with the difference that now the strong and electromagnetic potentials as well as the nucleon masses and energies are position dependent. Consequently, the final expression is similar to the free-space transition amplitude, and the uniform-matter result becomes, straightforwardly, a particular case of our expressions for the cross section.

We will not discuss in the present paper the important sources of suppression and enhancement due to in-medium correlation [30–34]. The coherent scattering of neutrinos by the pasta structure has been studied in [23,24]. The authors have analysed both the static structure factor and the dynamical response of the pasta and concluded that neutrino opacities are overestimated in the single heavy-nucleus approximation relative to the complete molecular dynamics simulations and that the dynamical response of pasta showed a substantial strength at low energies due to the contribution of collective modes. These effects are important in the low-energy neutrino region, when its wavelength is of the order of the cell size. Our main ob-

jective here is to understand how inhomogeneous matter affects the neutrino cross section through the mean-field effects under the conditions of incoherent neutrino scattering from individual nucleons.

In this paper we have considered only trapped neutrinos, and just electron neutrinos were taken into account in our calculations, since the other flavours are not expected to be present in the pasta region. However, we recognize that non-trapped neutrinos of all flavours can influence the total cross section and will be considered in a further investigation. As in [15], we have considered elastic scattering and neutrino absorption in our derivation. In other words, neutral current and charge-changing processes are included and their relative contribution to the total cross section is discussed. In what follows, an outline of the formalism is presented in sect. 2, numerical results and discussion are provided in sect. 3, and the conclusions are drawn in the final sect. 4. The details of the pasta phase calculation can be found in the cited references and some details of the cross section calculation are shown in the appendix.

2 Formalism and model parametrization

We start with a model Lagrangian density that includes electrons, neutrinos, nucleons, the sigma, omega, rho and delta meson fields and the electromagnetic interaction, given by [19,35]

$$\mathcal{L} = \sum_{i=p,n} \mathcal{L}_i + \mathcal{L}_\sigma + \mathcal{L}_\omega + \mathcal{L}_\rho + \mathcal{L}_{\omega\rho} + \mathcal{L}_\delta + \mathcal{L}_\gamma + \mathcal{L}_e + \mathcal{L}_\nu, \quad (1)$$

where the nucleon Lagrangian reads

$$\mathcal{L}_i = \bar{\psi}_i \left[\gamma_\mu i D^\mu - M^* \right] \psi_i, \quad (2)$$

with

$$iD^\mu = i\partial^\mu - \Gamma_v V^\mu - \frac{\Gamma_\rho}{2} \boldsymbol{\tau} \cdot \mathbf{b}^\mu - e\frac{1+\tau_3}{2} A^\mu, \quad (3)$$

$$M^* = M - \Gamma_s \phi - \Gamma_\delta \boldsymbol{\tau} \cdot \boldsymbol{\delta}. \quad (4)$$

The meson and electromagnetic Lagrangian densities are

$$\mathcal{L}_\sigma = \frac{1}{2} \left(\partial_\mu \phi \partial^\mu \phi - m_s^2 \phi^2 - \frac{\kappa}{3} \phi^3 - \frac{\lambda}{12} \phi^4 \right),$$

$$\mathcal{L}_\omega = \frac{1}{2} \left(-\frac{1}{2} \Omega_{\mu\nu} \Omega^{\mu\nu} + m_v^2 V_\mu V^\mu + \frac{\zeta}{12} g_v^4 (V_\mu V^\mu)^2 \right),$$

$$\mathcal{L}_\rho = \frac{1}{2} \left(-\frac{1}{2} \mathbf{B}_{\mu\nu} \cdot \mathbf{B}^{\mu\nu} + m_\rho^2 \mathbf{b}_\mu \cdot \mathbf{b}^\mu \right),$$

$$\mathcal{L}_\delta = \frac{1}{2} \left(\partial_\mu \boldsymbol{\delta} \partial^\mu \boldsymbol{\delta} - m_\delta^2 \boldsymbol{\delta}^2 \right),$$

$$\mathcal{L}_\gamma = -\frac{1}{4} F_{\mu\nu} F^{\mu\nu},$$

$$\mathcal{L}_{\omega\rho} = \Lambda \left(g_\rho^2 \mathbf{b}_\mu \cdot \mathbf{b}^\mu \right) \left(g_v^2 (V_\mu V^\mu) \right),$$

where $\Omega_{\mu\nu} = \partial_\mu V_\nu - \partial_\nu V_\mu$, $\mathbf{B}_{\mu\nu} = \partial_\mu \mathbf{b}_\nu - \partial_\nu \mathbf{b}_\mu - \Gamma_\rho (\mathbf{b}_\mu \times$

$\mathbf{b}_\nu)$ and $F_{\mu\nu} = \partial_\mu A_\nu - \partial_\nu A_\mu$. The electromagnetic coupling constant is given by $e = \sqrt{4\pi/137}$ and $\boldsymbol{\tau}$ is the isospin operator. Finally, the electron and neutrino Lagrangian densities read

$$\mathcal{L}_e = \bar{\psi}_e \left[\gamma_\mu (i\partial^\mu + eA^\mu) - m_e \right] \psi_e,$$

$$\mathcal{L}_\nu = \bar{\psi}_\nu \left[i\gamma_\mu \partial^\mu \right] \psi_\nu.$$

The weak-boson contributions to the above Lagrangians affect the solutions of the corresponding Euler-Lagrange equations in a completely negligible way due to their huge masses and relatively small energy range and are only relevant in order to obtain the neutrino cross sections.

The solutions of the corresponding Euler-Lagrange equations are obtained in the mean-field self-consistent Thomas-Fermi (TF) approximation, as explained in refs. [19,29]. We have considered two types of parametrizations: one with constant couplings Γ_i (NL) and another with density-dependent couplings (DD). In the last case, the terms proportional to κ, λ, ζ and Λ are set equal to zero. Within TF the system is considered locally uniform and the main output are the densities, which are position dependent. Explicitly, we have for the baryonic, scalar, isoscalar, scalar-isoscalar, electron and neutrino densities

$$\rho(\boldsymbol{r}) = \rho_p(\boldsymbol{r}) + \rho_n(\boldsymbol{r}) = \left\langle \hat{\psi}^\dagger \hat{\psi} \right\rangle;$$

$$\rho_s(\boldsymbol{r}) = \rho_{s_p}(\boldsymbol{r}) + \rho_{s_n}(\boldsymbol{r}) = \left\langle \hat{\bar{\psi}} \hat{\psi} \right\rangle;$$

$$\rho_3(\boldsymbol{r}) = \rho_p(\boldsymbol{r}) - \rho_n(\boldsymbol{r}) = \left\langle \hat{\psi}^\dagger \tau_3 \hat{\psi} \right\rangle;$$

$$\rho_{s3}(\boldsymbol{r}) = \rho_{sp}(\boldsymbol{r}) - \rho_{sn}(\boldsymbol{r}) = \left\langle \hat{\bar{\psi}} \tau_3 \hat{\psi} \right\rangle;$$

$$\rho_e(\boldsymbol{r}) = \left\langle \hat{\psi}_e^\dagger \hat{\psi}_e \right\rangle;$$

$$\rho_\nu(\boldsymbol{r}) = \left\langle \hat{\psi}_\nu^\dagger \hat{\psi}_\nu \right\rangle;$$

with

$$\rho_i(\boldsymbol{r}) = \frac{\gamma}{(2\pi)^3} \int d^3k \left(\eta_{ki}(T) - \bar{\eta}_{ki}(T) \right), \quad i = p, n, e, \nu; \quad (5)$$

$$\rho_{si}(\boldsymbol{r}) = \frac{\gamma}{(2\pi)^3} \int d^3k \, \frac{M_i^*}{E_i^*} \left(\eta_{ki}(T) + \bar{\eta}_{ki}(T) \right), \quad i = p, n; \quad (6)$$

where $E^* = \sqrt{k^2 + M^{*2}}$, $\boldsymbol{k}$ is the momentum and γ is the spin multiplicity ($\gamma = 2$ for protons, neutrons and electrons and $\gamma = 1$ for neutrinos). For a given temperature T, the distributions are

$$\eta_{ki}(T) = \{ \exp [(E_i - \mu_i)/T] + 1 \}^{-1};$$

$$\bar{\eta}_{ki}(T) = \{ \exp [(\bar{E}_i - \bar{\mu}_i)/T] + 1 \}^{-1}; \quad (7)$$

with E_i $(\bar{E}_i)$ and μ_i $(\bar{\mu}_i)$ being the particle (antiparticle) energy and chemical potential, respectively. The particle (antiparticle) energy depends on the mesonic fields and is position dependent.

Once the densities are determined we calculate the total neutrino cross section (σ). We follow here the procedure discussed in [15]. For a collision $1 + 2 \longrightarrow 3 + 4$ we write

$$
\begin{aligned}
\sigma = 2G_F{}^2 \int \mathrm{d}^3 r \int \frac{\mathrm{d}^3 k_2}{(2\pi)^3} \int \frac{\mathrm{d}^3 k_3}{(2\pi)^3} \int \frac{\mathrm{d}^3 k_4}{(2\pi)^3} \frac{(2\pi)^4}{|\vec{v}_1 - \vec{v}_2|} \\
\cdot \delta^4 (P_1 + P_2 - P_3 - P_4)\eta_2(T)(1 - \eta_3(T))(1 - \eta_4(T)) \\
\cdot \Bigg\{ (\mathcal{V} + \mathcal{A})^2 (1 - v_2 \cos(\theta_{12}))(1 - v_4 \cos(\theta_{34})) \\
+ (\mathcal{V} - \mathcal{A})^2 (1 - v_4 \cos(\theta_{14}))(1 - v_2 \cos(\theta_{23})) \\
- \frac{M_2^* M_4^*}{E_2^* E_4^*}(\mathcal{V}^2 - \mathcal{A}^2)(1 - \cos(\theta_{13})) \Bigg\}. \quad (8)
\end{aligned}
$$

$v_i = |\mathbf{k}_i|/E_i^*$, G_F is the Fermi constant and $\mathcal{V}$, $\mathcal{A}$ are the weak-current vector and axial vector couplings, respectively, and depend on the target particle and on the exchanged weak boson. For the neutrino-electron (neutrino) cross section we replace M^* by m_e (zero). The factors $(1 - \eta_3(T))$ and $(1 - \eta_4(T))$ are due to final-state Pauli blocking effects. We have considered here scattering through neutral current and charge-changing processes as well as neutrino absorption by the neutrons. The explicit expressions and definitions for each case are shown in the appendix. Through the analysis of those expressions we may conclude that the integrand in the cross section is $\mathbf{r}$-dependent, since the potentials and the effective mass are position dependent. Note that the same expression can be used for the calculation of the cross section in the infinite nuclear matter, for which the potentials and effective mass are not $\mathbf{r}$-dependent. Also, the above expression for the cross section has no approximations of the type $E \approx M$, which is usually taken for baryonic targets, nor of the type $E \approx |\vec{k}|$ for electron targets.

The nucleon internal structure was taken into account in our calculation, just multiplying the couplings $\mathcal{V}$ and $\mathcal{A}$ by the vector and axial-vector nucleon form factors as explained, for instance, in [36,37] and explicitly written in the appendix.

The neutrino mean free path is then obtained considering the cross section for a Wigner-Seitz cell divided by its volume

$$
\lambda = \left(\frac{\sigma}{V} \right)^{-1}. \quad (9)
$$

3 Results and discussion

In what follows we show our main results for the pasta phase, using both Lagrangian parametrizations with constant and density-dependent couplings, as explained before. For the parametrizations with non-linear terms in the mesonic sector and constant couplings, we choose the GM3 [38], NL3 [39], NL3$\omega\rho$ [40] and the FSUGold [41] sets of parameters. The sets NL3 and NL3$\omega\rho$ only differ in the density dependence of the symmetry energy and will allow the discussion of the effect of this quantity on the neutrino mean free path. For the density-dependent case we take the TW [42] and the van Dalen *et al.* [43]

Table 1. Model properties for infinite symmetric nuclear matter at zero temperature and saturation density: the saturation density ρ_0, the binding energy E_B/A, the incompressibility K, the nucleon effective mass M^*, the symmetry energy a_{sym} and its slope L.

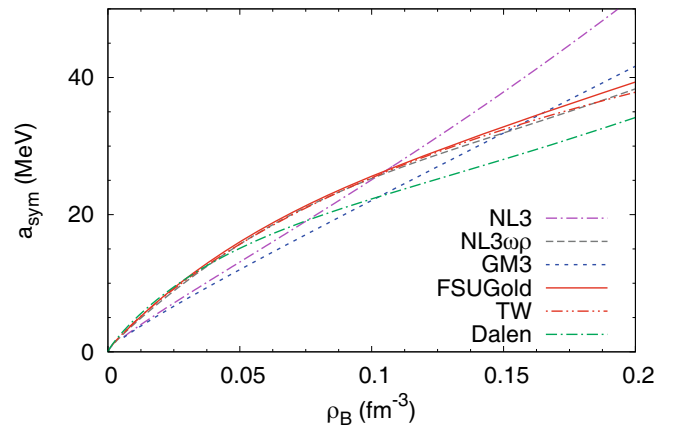| | ρ_0 | E_B/A | K | M^*/M | a_{sym} | L |
	(fm^{-3})	(MeV)	(MeV)		(MeV)	(MeV)
FSUGold	0.148	16.299	271.76	0.6	37.4	60.4
GM3	0.153	16.3	240	0.78	32.5	89.66
NL3	0.148	16.3	272	0.6	37.4	118.3
NL3$\omega\rho$						
($l_v = 0.3$)	0.148	16.3	272	0.6	31.7	55.2
Dalen	0.178	16.25	337	0.68	32.11	57
TW	0.153	16.247	240	0.555	33.39	55.3

Fig. 1. Symmetry energy as a function of the total baryonic density for all the models used in the present work.

sets. The last one was recently taken for neutrino mean-free-path studies [20]. Table 1 shows the properties of the models for symmetric nuclear matter at saturation density ρ_0 and zero temperature, and in fig. 1 we have plotted the symmetry energy of the models *versus* the density, a quantity that will be necessary to discuss the results in the following. Models Dalen, GM3 and NL3 have a smaller symmetry energy in all or part of the density range below $0.1\,\mathrm{fm}^{-3}$. A smaller symmetry energy allows the system to have a larger isospin asymmetry. As we will see next these three models are precisely the ones with smaller proton fractions in the pasta phase matter, and this will induce a noticeable effect on the neutrino mean free path.

The free energy per particle obtained with the FSUGold parametrization for β-equilibrium matter with trapped neutrinos for a fixed fraction of leptons $Y_L = 0.2$ is shown in fig. 2, where the different geometries are identified by different colors. The uniform-matter result is also shown, and, as expected, has a larger free energy than the pasta phases. Although the transition densities between geometries may differ slightly, depending on the parametrization used [44], the qualitative behaviour does not change significantly compared to the case shown. The
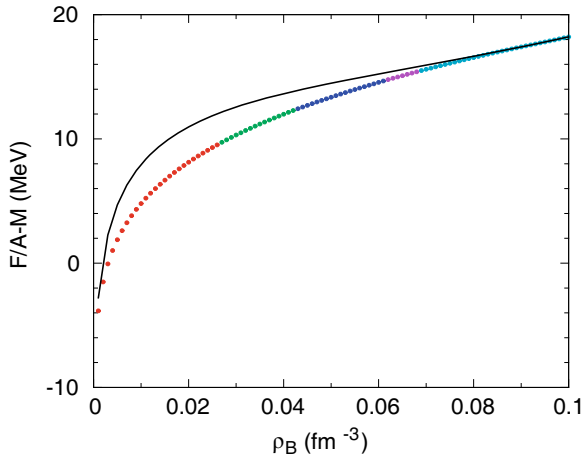
Fig. 2. Free energy per barion as a function of the total baryonic density using the FSUGold parametrization for uniform matter (black) and the pasta phase matter within droplet (red), rod (green), slab (blue), tube (purple) and bubble (light blue) geometries. The temperature was taken as $T = 3\,\mathrm{MeV}$. M is the free nucleon mass.
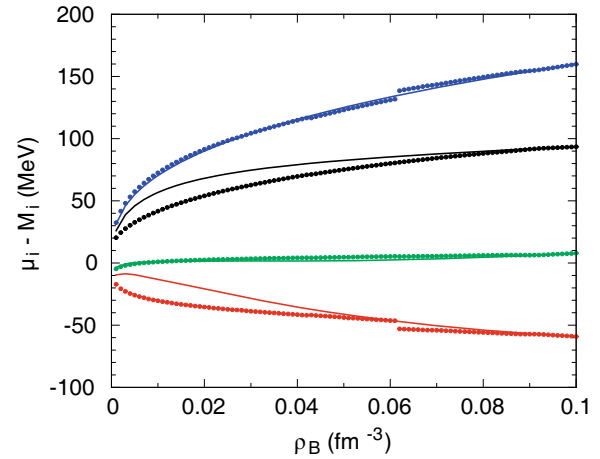

Fig. 4. Chemical potential as a function of the total baryonic density using the FSUGold parametrization for the pasta phase (points) compared to homogeneous matter (lines) for the neutrons (green), protons (red), electrons (blue) and neutrinos (black). The temperature was taken as $T = 3\,\mathrm{MeV}$ and M_i is the rest mass of the corresponding particle.
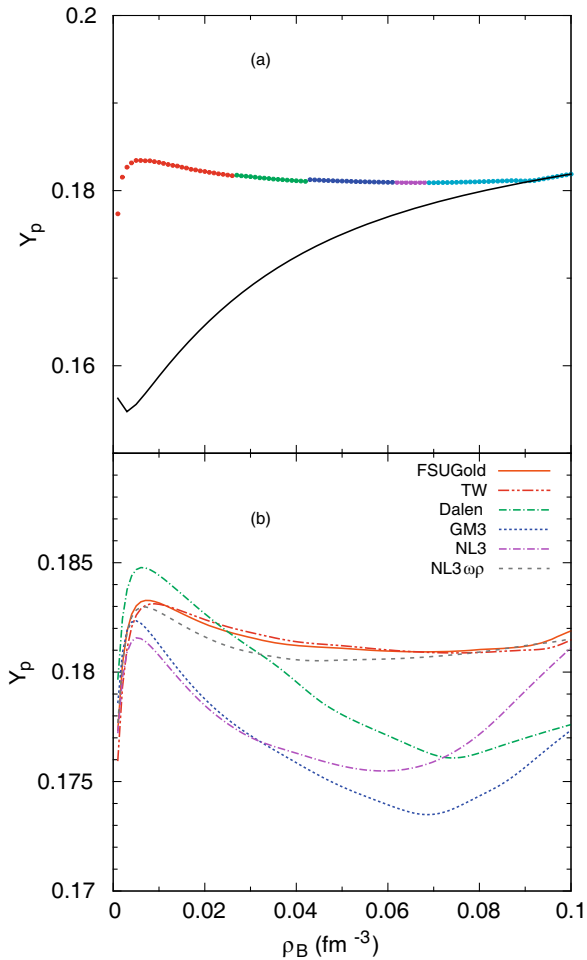

Fig. 3. Proton fraction as a function of the total baryonic density, (a) using the FSUGold parametrization for uniform matter (black) and the pasta phase matter within droplet (red), rod (green), slab (blue), tube (purple) and bubble (light blue) geometries, (b) for all the models and the pasta phase matter. The temperature was taken as $T = 3\,\mathrm{MeV}$.

density profile of the particles inside a single cell, within our Thomas-Fermi calculation, are shown, for instance, in ref. [19].

Figures 3(a) and 4 display, respectively, the proton fraction and the chemical potential for all particles involved using again the FSUGold parametrization to describe neutrino trapped β-equilibrium matter. All these results were obtained for a temperature $T = 3\,\mathrm{MeV}$. One important effect of the clusterization of matter is the increase of the mean proton fraction.

An effect of the larger proton fraction on neutral matter with a fixed lepton fraction is the reduction of the neutrino fraction and, consequently, the neutrino chemical potential as seen in fig. 4. At low temperatures, when degeneracy effects are important, a smaller neutrino chemical potential will give rise to larger mean free paths, and neutrinos will diffuse out of the star more easily. In fig. 3(b) the pasta phase proton fraction is plotted for all the models studied. These results reflect the density dependence of the symmetry energy of the respective models: a smaller proton fraction occurs for the models with a smaller symmetry energy at the baryonic density range of interest. In particular the three models with a smaller proton fraction are GM3, Dalen and NL3, the three models that have the smaller symmetry energy for $0.05 < \rho < 0.1\,\mathrm{fm}^{-3}$.

The individual mean free path contribution for each particle type is shown in fig. 5 as a function of ρ_B, for the FSUGold and $T = 3\,\mathrm{MeV}$. The curves labelled proton, neutron and neutrino are the contributions for elastic neutral-current scattering, while the curve labelled electron has also an elastic contribution from charged-current scattering. The dominance of the absorption process on the total cross section is clear, as was also concluded in previous calculations [15], except for very low densities, in the droplet region, where the neutron elastic scattering competes with the absorption process.
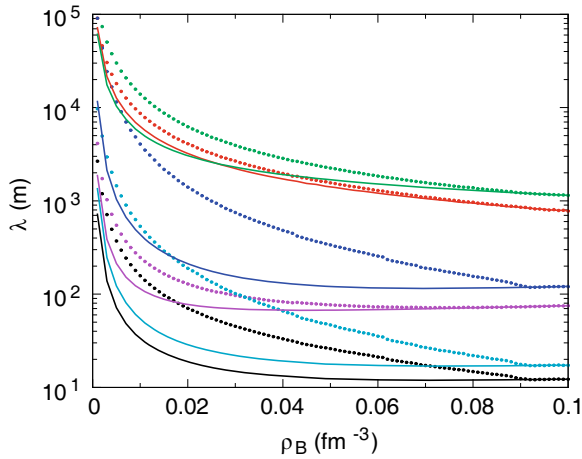
Fig. 5. Mean free path as a function of the total baryonic density using the FSUGold parametrization for the pasta phase matter (dotted lines) compared to homogeneous matter (full lines). Individual contributions for the electrons (red), neutrinos (green), protons (blue) and neutrons (purple). The absorption contribution is shown in light blue and the total value is shown in black. The temperature was taken as $T = 3\,\mathrm{MeV}$ and $E_\nu = \mu_\nu$.

Fig. 6. Mean free path as a function of the total baryonic density comparing several parametrizations for the pasta phase matter. TW (red), Dalen (green), GM3 (blue), NL3 (purple), NL3$\omega\rho$ (grey) and FSUGold (orange). The FSUGold for homogeneous matter (black) is also shown. The temperature was taken as $T = 3\,\mathrm{MeV}$ and $E_\nu = \mu_\nu$.

Fig. 7. The neutrino mean free path as a function of the total baryonic density within FSUGold parametrization for the pasta phase (points) compared to homogeneous matter (lines) for $T = 3\,\mathrm{MeV}$ (black), $T = 5\,\mathrm{MeV}$ (red) and $T = 7\,\mathrm{MeV}$ (blue) and $E_\nu = \mu_\nu$.

Considering the scattering of the neutrinos from the individual nucleons of the pasta, as done in the present calculation, we see that the mean free path increases a lot in comparison with the homogeneous-matter case, mainly at low densities, when the clusterized matter presents much larger proton fractions, and, therefore, the absorption process and the scattering by neutrons are less likely to occur: the neutrino couples more strongly to the neutron than to the proton. Other causes are related to the nucleon distributions. Nucleons are concentrated in clusters and the larger Fermi momenta of nucleons in the cluster give rise to stronger Pauli blocking effects. Each WS cell contains, besides the cluster, a low-density nucleon background gas which has a smaller contribution to the total cross section than normal homogeneous matter. At the upper bound of the inner crust the neutron and proton densities of the background gas and the clusters get closer to homogeneous-matter distribution and the same should happen to the neutrino mean free path. In fig. 5 the difference between homogeneous matter and pasta phase NMFP is shown for the different processes: the absorption component is strongly affected, due to a reduction of the number of the neutrons. The bigger differences encountered for the scattering of protons, as compared to the neutrons, come from the differences in the chemical potential (see fig. 4), due to the Coulomb potential and due to the details of the position dependence of the Fermi momentum in the non-homogeneous case.

The sensitivity of the total mean free path (λ_T) to the parametrization used is presented in fig. 6 together with the uniform-matter result obtained with the FSUGold parameter set. At low densities the models do not differ much. This is expected since all models have similar behaviours, in particular, the proton fraction is almost the same in all of them, see [44]. The differences occur
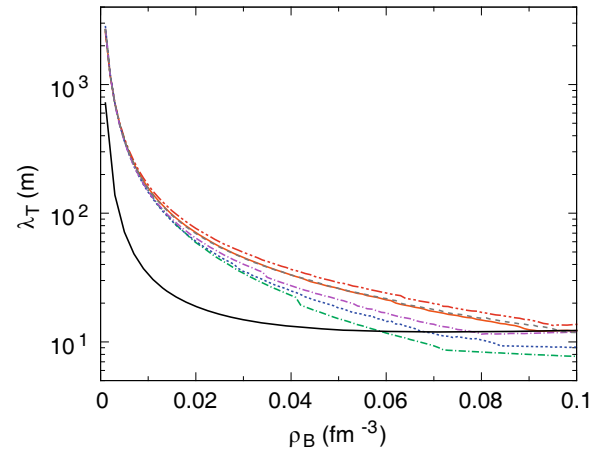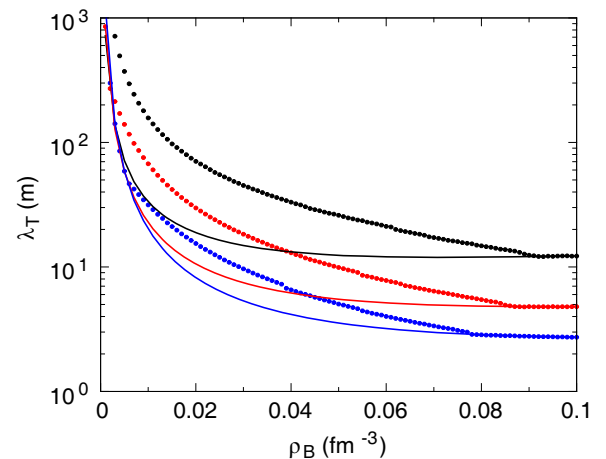
precisely after the onset of the non-spherical pasta structures, $\rho_B > 0.02\,\mathrm{fm}^{-3}$, which is a range of densities that is sensitive to the density dependence of the symmetry energy. GM3 and Dalen have the lowest mean free paths: for a fixed lepton fraction, a smaller proton fraction (see fig. 3) corresponds to a smaller electron fraction, which increases the neutrino fraction and the neutrino chemical potential. All these facts favour the absorption process, and consequently the NMFP is smaller. Comparing NL3 and NL3$\omega\rho$ we also conclude that the softer density dependence of the symmetry energy gives rise to larger mean free paths.

The dependence of the results on the temperature is shown in fig. 7. Temperature has a strong effect on the pasta structures which start to melt. Although within a
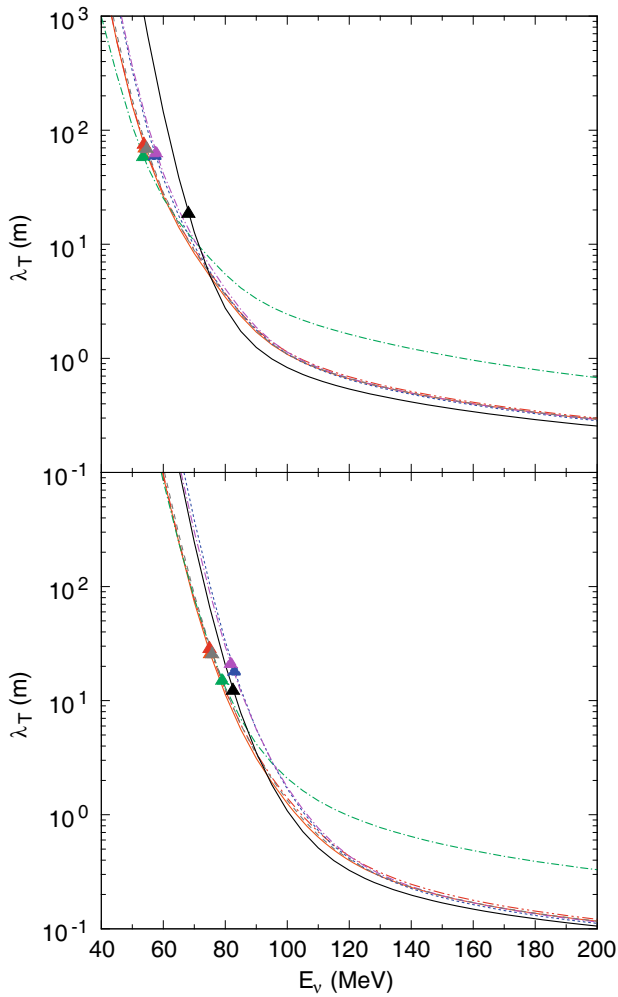
Fig. 8. Neutrino mean free path as a function of the neutrino incident energy for the pasta phase comparing the parametrizations TW (red), Dalen (green), GM3 (blue), NL3 (purple), NL3$\omega\rho$ (grey), FSUGold (orange) and FSUGold homogeneous matter (black). The temperature was taken as $T = 3$ MeV with $\rho_B = 0.02$ fm^{-3} (upper panel) and $\rho_B = 0.05$ fm^{-3} (lower panel). The triangles indicate the NMFP at the neutrino chemical potential, μ_ν, of the respective model.
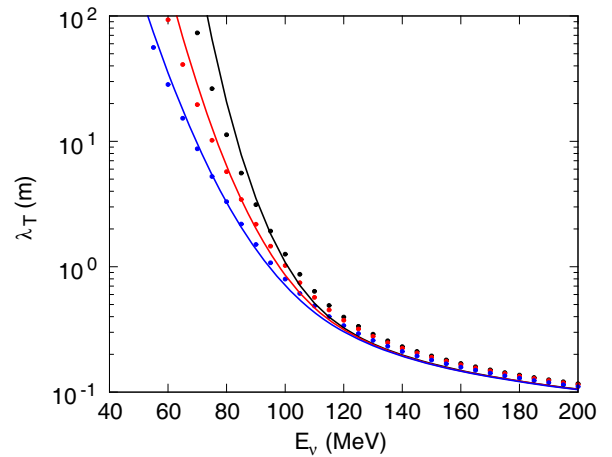

Fig. 9. Neutrino mean free path as a function of the neutrino incident energy for the pasta phase with $\rho_B = 0.05$ fm^{-3} and $T = 3$ MeV (black), $T = 5$ MeV (red) and $T = 7$ MeV (blue). The points represent pasta and the full lines homogeneous matter.

TF calculation pasta structures still exist at $T > 10$ MeV, according to [45], if thermal fluctuations are considered the Wigner-Seitz cell structure is supposed to melt for $T > 7$ MeV. Temperature increases drastically the background gas of dripped particles in the Wigner-Seitz cells and, therefore, the larger the temperature the closer the pasta mean free path comes to the homogeneous-matter one. The reduction of the mean free path with the increase of the temperature is also expected, because the Fermi-Dirac distributions are smoothed when the temperature increases, making Pauli blocking effects weaker and allowing more reactions.

In fig. 8 the NMFP is plotted as a function of the neutrino incident energy for the pasta phase with $\rho_B = 0.02$ fm^{-3} and $\rho_B = 0.05$ fm^{-3}. We also include the homogeneous-matter result obtained within FSUGold. The values of λ at the neutrino chemical potential are indicated with triangles. We expect that the neutrinos with energy around the chemical potential will provide the main contribution to the dispersion of energy in the system, because at low temperatures the system is practically degenerate and Pauli blocking factors will weaken other contributions. The highly degenerate regime is expected for $\mu_i/T \gg 1$, and this condition is essentially true for temperatures below the pasta melting temperature. For $\rho_B = 0.05$ fm^{-3}, the gas of dripped neutrons is denser and the proton fraction closer to the homogeneous one (see the blue region in fig. 3(a) in comparison with the red region). Consequently, the NMFP comes closer to the homogeneous-matter result.

In fig. 9 we consider again $\rho_B = 0.05$ fm^{-3}, corresponding to the slab geometry, at three different temperatures. As expected, with the increase of the neutrino incident energy, temperature effects disappear. As we can see from both figs. 8 and 9, the NMFP for neutrinos with lower energy are smaller in the pasta and neutrinos with larger energy have a greater NMFP in the pasta. This is because at low energies Pauli blocking suppresses the interaction of neutrinos with nucleons inside the cluster or in the homogeneous matter, but the collisions with the surface nucleons of the clusters are still possible. As the energy of the neutrino increases, the Pauli blocking effects are weaker and the NMFP in the homogeneous matter is smaller as discussed above.

Finally, in figs. 10, 11 and 12, we present our results for the neutrino diffusion coefficients, as defined for instance in [15]. We also show the homogeneous-matter diffusion coefficients and they agree with the coefficients calculated in [15], for the density region considered here. For the pasta we obtain bigger diffusion coefficients and these results reflect the bigger NMFP in the pasta matter. Compared to the corresponding results in ref. [9], we see a systematic qualitative inversion in the sense that our pasta coefficients remain always bigger than the homogeneous-matter counterpart. In fact, compared to the calculations shown in [9] our method provides a spatial distribution of
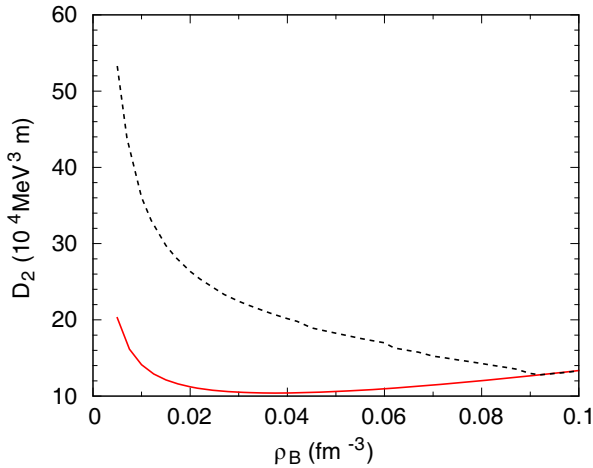
Fig. 10. Neutrino diffusion coefficient D2 as a function of the baryonic density for the pasta phase (dashed line) and for homogeneous matter (full line) and $T = 3\,\text{MeV}$.

Fig. 11. Neutrino diffusion coefficient D3 as a function of the baryonic density for the pasta phase (dashed line) and for homogeneous matter (full line) and $T = 3\,\text{MeV}$.
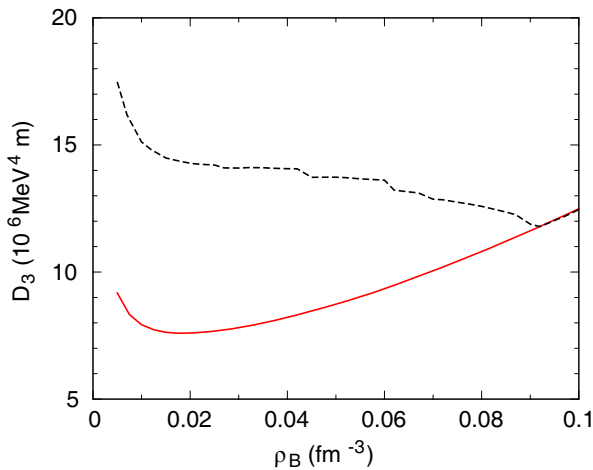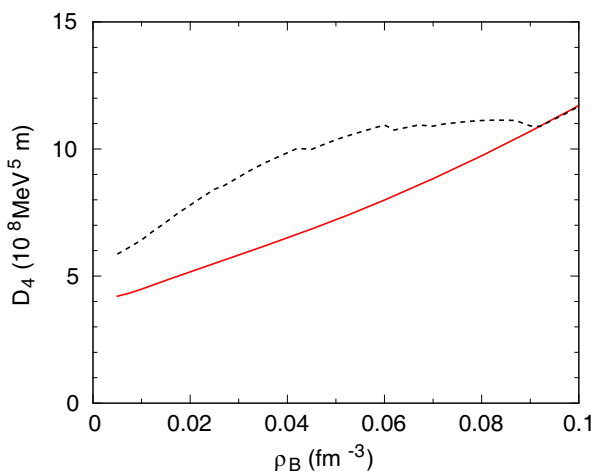

Fig. 12. Neutrino diffusion coefficient D4 as a function of the baryonic density for the pasta phase (dashed line) and for homogeneous matter (full line) and $T = 3\,\text{MeV}$.

the matter inside the cell which is automatically taken into account in the cross section calculation, and the approximations used in [9] have not been implemented in the present study. The homogeneous diffusion coefficients in [9] are one order of magnitude larger than the ones in [15] and the ones we have obtained for densities of the order of $\sim 0.05\,\text{fm}^{-3}$.

4 Conclusions

We have studied the effect of the pasta phase, occurring in the inner crust of a neutron star, on the neutrino mean free path (NMFP). The pasta phases have been obtained within a self-consistent Thomas-Fermi approximation, as explained in refs. [19,29]. Several relativistic nuclear models have been used to describe the pasta phase, both with non-linear meson terms and constant couplings, and with density-dependent couplings. In particular, we were interested in discussing whether the properties of the models, such as the density dependence of the symmetry energy, would have some influence on the NMFP. We have also studied the effect of the temperature. It should be stressed, however, that the present work is restricted to density and temperature ranges for which the pasta phases exist, *e.g.* $T \lesssim 10\,\text{MeV}$ and $\sim 0.0002\,\text{fm}^{-3} < \rho < \rho_t$ where the density at the crust-core transition $\rho_t \sim \rho_0/2$. We have considered both charged- and neutral-current reactions. It has been shown that the absorption process dominates the NMFP, but other processes cannot be discarded.

At low density, $\rho_B < 0.02\,\text{fm}^{-3}$, where the pasta phases obtained within the different parametrizations have similar properties [44], the NMFP has a small dependence on the parametrization. As the density increases, namely at the layers close to the upper border of the inner crust, the dependence on the parametrization becomes more important. With a larger proton fraction, the absorption process is less likely to occur. Consequently, models with larger proton fractions result in larger NMFP. The proton fraction is closely related to the density dependence of the symmetry energy, and, therefore, the effect of this property on the NMFP is not negligible.

Besides the effect of the larger proton fraction of the non-homogeneous phases, also Pauli blocking effects increase the NMFP with respect to homogeneous matter. In fact, the scattering processes are strongly suppressed by Pauli blocking effects inside the cluster, where the Fermi energy is larger than in homogeneous matter. On the other hand the background gas of each WS cell contains a too small number of nucleons to have a significant contribution to the total cross section. At the temperatures we have considered, the neutrinos are degenerate, and the Pauli blocking factors ensure that only neutrinos close to the Fermi energy are involved in the scattering processes. Also the fact that degenerate neutrinos in the presence of pasta phases have smaller energies than in homogeneous matter results in larger NMFP. When the density or the temperature increases, originating the melting of the pasta phases, both the pasta and the homogeneous-matter NMFP get closer.

We have shown that the NMFP is larger, by as much as an order of magnitude, in the presence of pasta phases than when considering homogeneous β-equilibrium matter at the same density. This effect will give rise to shorter neutrino emission time-scales. Also, this means that if the clusterized matter is accounted for adequately in a supernovae simulation code at the neutrino trapped stage, the energy transferred to low-density layer that settles onto the PNS surface is more efficient. Our results imply that the effects of the pasta phase cannot be neglected when calculating the NMFP at baryonic densities below $0.1\,\mathrm{fm}^{-3}$ and temperatures below $10\,\mathrm{MeV}$. The parametrization used to describe the pasta phase has also influence on the results, in particular, due to the density dependence of the symmetry energy.

We have not considered coherent scattering of the neutrinos from the pasta clusters as done in [7,8]. These processes are important when all neutrons respond coherently and can cause an important reduction of the NMFP for neutrino energies $E_\nu \lesssim 80\,\mathrm{MeV}$, compared to free neutrino-neutron scattering [23,24]. Coherent effects have to be considered if the neutrino wavelength is comparable to the radius of the cluster. Pasta phase calculations of the inner crust give $10 < R_{WS} < 30\,\mathrm{fm}$, where R_{WS} is the Wigner-Seitz cell radius and for densities above $0.01\,\mathrm{fm}^{-3}$, see [19]. In [8], coherent effects have been calculated within a liquid-drop model approach and a quantum molecular dynamics calculation. The structure function shows a peak at 30–40 MeV, for $T = 1\,\mathrm{MeV}$ and a proton fraction equal to 0.3, and decreases smoothly for larger neutrino energies approaching the incoherent neutrino scattering from individual-nucleons result. It was also shown that temperature broadens and reduces the peak due to thermal fluctuations. The scattering processes discussed in the present work are important when the neutrinos are scattered by the individual nucleons that form the pasta cluster and, therefore, for neutrinos with a larger energy. Also, as we are concerned with the neutrino trapped phase corresponding to the initial deleptonization of a protoneutron star, neutron superfluidity plays no role since the temperatures involved are above the pairing critical temperature [46,47].

Appendix A.

According to eq. (8), with $\boldsymbol{k}_1 = k_1 \hat{z}$ and after the $\boldsymbol{k}_4$ integration in the scattering case

$$
\sigma_{scat} = 2\frac{G_F{}^2}{(2\pi)^5} \int \mathrm{d}^3 r \int \mathrm{d}^3 k_2 \int_0^\pi \sin(\theta_3)\mathrm{d}\theta_3 \int_0^{2\pi} \mathrm{d}\phi_3\, k_3^2
$$

$$
\cdot \frac{\eta_2(T)(1-\eta_3(T))(1-\eta_4(T))}{|\boldsymbol{v}_1 - \boldsymbol{v}_2|}
$$

$$
\cdot \frac{k_1 + E_2^* - k_3}{k_1(1-\cos(\theta_3)) + E_2^* - k_2\cos(\theta_{23})}
$$

$$
\cdot \Big\{ (c_V + c_A)^2 (1 - v_2\cos(\theta_2))(1 - f_{123})
$$

$$
+ (c_V - c_A)^2 (1 - v_2\cos(\theta_{23}))(1 - g_{123})
$$

$$
- \frac{M_2^* M_4^*}{E_2^* E_4^*}(c_V^2 - c_A^2)(1 - \cos(\theta_3)) \Big\}, \tag{A.1}
$$

with

$$
f_{123} = \frac{k_1\cos(\theta_3) + k_2\cos(\theta_{23}) - k_3}{E_4^*} \,;
$$

$$
g_{123} = \frac{k_1 + k_2\cos(\theta_2) - k_3\cos(\theta_3)}{E_4^*} \,;
$$

$$
k_3 = \frac{k_1(E_2^* - k_2\cos(\theta_2))}{k_1 + E_2^* - k_1\cos(\theta_3) - k_2\cos(\theta_{23})} \,.
$$

For the absorption, we find

$$
\sigma_{abs} = 2\frac{G_F{}^2}{(2\pi)^5} \int \mathrm{d}^3 r \int \mathrm{d}^3 k_2 \int_0^\pi \sin(\theta_3)\mathrm{d}\theta_3 \int_0^{2\pi} \mathrm{d}\phi_3\, k_3^2
$$

$$
\cdot \frac{\eta_2(T)(1-\eta_3(T))(1-\eta_4(T))}{|\boldsymbol{v}_1 - \boldsymbol{v}_2|}
$$

$$
\cdot \frac{\sqrt{m_e^2 + k_3^2}(C - \sqrt{m_e^2 + k_3^2})}{Ck_3 - F\sqrt{m_e^2 + k_3^2}}
$$

$$
\cdot \Big\{ (g_V + g_A)^2 (1 - v_2\cos(\theta_2))(1 - f_{123})
$$

$$
+ (g_V - g_A)^2 (1 - g_{123})(1 - v_2\cos(\theta_{23}))
$$

$$
- \frac{M_2^* M_4^*}{E_2^* E_4^*}(g_V^2 - g_A^2)(1 - \cos(\theta_3)) \Big\}, \tag{A.2}
$$

where now

$$
k_3 = -\frac{2F(C^2 + m_e^2 - D)}{4(k_1\cos(\theta_3) + k_2\cos(\theta_{23}))^2 - 4C^2}
$$

$$
- \frac{\sqrt{16m_e^2 C^2 F^2 + 4C^2(C^2 + m_e^2 - D)^2 - 16m_e^2 C^4}}{4F^2 - 4C^2} \,;
$$

$$
D = (\boldsymbol{k}_1 + \boldsymbol{k}_2)^2 + M_4^* ;
$$

$$
C = k_1 + E_2^* - g_\rho b_0 ;
$$

$$
F = k_1\cos(\theta_3) + k_2\cos(\theta_{23}). \tag{A.3}
$$

The constants are:

neutrino-proton: $c_V = 1/2 - 2\sin^2(\theta_w)$; $c_A = 1.23/2$,
neutrino-neutron: $c_V = -1/2$; $c_A = -1,23/2$,
neutrino-electron: $c_V = 1/2 + 2\sin^2(\theta_w)$; $c_A = 1/2$,
neutrino-neutrino: $c_V = \sqrt{2}$; $c_A = \sqrt{2}$,
absorption: $g_V = C$; $g_A = -1.23C$

with $C = 0.973$ and $\sin^2(\theta_w) = 0.230$. Each neutrino-electron and neutrino-neutrino collisions can be represented by two (first-order) Feynman diagrams, in such a way that the values of c_V and c_A can be re-defined to accommodate the different cross section contributions in a single expression, as given above. Also, we define

$$
E^* = \sqrt{\boldsymbol{k}^2 + M^{*2}} \,.
$$

For the particle energy we have for the nucleon

$$E_i = E^* + \Gamma_v V_0(\boldsymbol{r}) \pm \frac{1}{2}\Gamma_\rho b_0(\boldsymbol{r}) + eA_0(\boldsymbol{r})$$

in the NL parametrization case and

$$E_i = E^* + \Gamma_v V_0(\boldsymbol{r}) \pm \frac{1}{2}\Gamma_\rho b_0(\boldsymbol{r}) + eA_0(\boldsymbol{r})$$
$$+ \frac{\partial \Gamma_v}{\partial \rho_B}\rho_B V_0 + \frac{\partial \Gamma_\rho}{\partial \rho_B}\frac{\rho_3}{2}b_0 + \frac{\partial \Gamma_\delta}{\partial \rho_B}\rho_{s3}\delta_0 - \frac{\partial \Gamma_s}{\partial \rho_B}\rho_s\phi_0$$

in the DD case. The plus sign in the equations above has to be chosen for the proton and the minus sign for the neutron. Also, V_0, ϕ_0, b_0 and δ_0 are the time-like components of the meson fields. For the electron

$$E_e = \sqrt{k^2 + m_e^2} - eA_0(\boldsymbol{r}); \qquad M^* \to m_e$$

and for the neutrino:

$$E_\nu = k; \qquad M^* \to 0.$$

Finally, in order to take into account the finite size of the nucleon, we have multiplied the constants g_V (g_A), or c_V (c_A), by the corresponding form factor. Using the parametrizations as explained in [36,37], we have taken a common structure factor given by

$$\left(1 + \frac{4.97q^2}{4M^2}\right)^{-2}, \tag{A.4}$$

where $q \equiv |\boldsymbol{q}| = |\boldsymbol{p}_1 - \boldsymbol{p}_3|$.

References

1. B. Bodmann *et al.*, Phys. Lett. B **332**, 251 (1994).
2. R. Imlay *et al.*, Nucl. Phys. A **629**, 531c (1998).
3. A. Aguilar-Arevalo *et al.*, Phys. Rev. Lett. **100**, 032301 (2008)
4. T. Walton *et al.*, Phys. Rev. D **91**, 071301 (2015).
5. Christophe Praet, *Modelling Quasi-Free Neutrino Nucleus Reactions for Accelerator-Based Experiments* (Universiteit Gent, Gent, 2009).
6. T. Maruyama, T. Tatsumi, T. Endo, S. Chiba, Recent Dev. Phys. **7**, 1 (2006).
7. C.J. Horowitz, M.A. Perez-Garcia, J. Carriere, D.K. Berry, J. Piekarewicz, Phys. Rev. C **70**, 065806 (2004).
8. Hidetaka Sonoda, Gentaro Watanabe, Katsuhiko Sato, Tomoya Takiwaki, Kenji Yasuoka, Toshikazu Ebisuzaki, Phys. Rev. C **75**, 042801 (2007).
9. M.D. Alloy, D.P. Menezes, Phys. Rev. C **83**, 035803 (2011).
10. H.Th. Janka, K. Langanke, A. Marek, G. Martinez-Pinedo, B. Muller, Phys. Rep. **442**, 38 (2007).
11. S.W. Bruenn, Astrophys. J. Suppl. **58**, 771 (1985).
12. G. Martinez-Pinedo, T. Fischer, A. Lohs, L. Huther, Phys. Rev. Lett. **109**, 241104 (2012).
13. J.A. Pons, S. Reddy, M. Prakash, J.M. Lattimer, J.A. Miralles, Astrophys. J. **513**, 780 (1999).
14. T. Fischer, G. Martinez-Pinedo, M. Hempel, M. Liebendo, Phys. Rev. D **85**, 083003 (2012).
15. S. Reddy, M. Prakash, J.M. Lattimer, Phys. Rev. D **58**, 013009 (1998).
16. T. Fischer, M. Hempel, I. Sagert, Y. Suwa, J. Schaffner-Bielich, Eur. Phys. J. A **50**, 46 (2014).
17. M.B. Tsang *et al.*, Phys. Rev. C **86**, 015803 (2012).
18. T. Maruyama, T. Tatsumi, D.N. Voskresensky, T. Tanigawa, S. Chiba, Phys. Rev. C **72**, 015802 (2005).
19. S.S. Avancini, D.P. Menezes, M.D. Alloy, J.R. Marinelli, M.M.W. de Moraes, C. Providência, Phys. Rev. C **78**, 015802 (2008).
20. P. Grygorov, P. Gogelein, H. Muther, J. Phys. G: Nucl. Part. Phys. **37**, 075203 (2010).
21. M. Okamoto, T. Maruyama, K. Yabana, T. Tatsumi, Phys. Lett. B **713**, 284 (2012).
22. M. Okamoto, T. Maruyama, K. Yabana, T. Tatsumi, Phys. Rev. C **88**, 025801 (2013).
23. C.J. Horowitz, M.A. Prez-Garcia, J. Piekarewicz, Phys. Rev. C **69**, 045804 (2004).
24. C.J. Horowitz, M.A. Prez-Garcia, D.K. Berry, J. Piekarewicz, Phys. Rev. C **72**, 035801 (2005).
25. Gentaro Watanabe, Toshiki Maruyama, Katsuhiko Sato, Kenji Yasuoka, Toshikazu Ebisuzaki, Phys. Rev. Lett. **94**, 031101 (2005).
26. Hidetaka Sonoda, Gentaro Watanabe, Katsuhiko Sato, Kenji Yasuoka, Toshikazu Ebisuzaki, Phys. Rev. C **77**, 035806 (2008).
27. Gentaro Watanabe, Hidetaka Sonoda, Toshiki Maruyama, Katsuhiko Sato, Kenji Yasuoka, Toshikazu Ebisuzaki, Phys. Rev. Lett. **103**, 121101 (2009).
28. A.S. Schneider, C.J. Horowitz, J. Hughto, D.K. Berry, Phys. Rev. C **88**, 065807 (2013).
29. S.S. Avancini, S. Chiacchiera, D.P. Menezes, C. Providência, Phys. Rev. C **82**, 055807 (2010).
30. N. Iwamoto, C.J. Pethick, Phys. Rev. D **25**, 313 (1982).
31. C.J. Horowitz, K. Wehrberger, Nucl. Phys. A **531**, 665 (1991).
32. C.J. Horowitz, K. Wehrberger, Phys. Rev. Lett. **66**, 272 (1991).
33. G. Fabbri, F. Matera, Phys. Rev. C **54**, 2031 (1996).
34. Sanjay Reddy, Madappa Prakash, James M. Lattimer, J.A. Pons, Phys. Rev. C **59**, 2888 (1999).
35. C.A. Graeff, J.R. Marinelli, J. Phys.: Conf. Ser. **312**, 092027 (2011).
36. J.R. Marinelli, C.A. Graeff, EPJ Web of Conferences **66**, 02068 (2014).
37. S. Galster, H. Klein, J. Moritz, K.H. Schmidt, D. Wegener, J. Bleckwenn, Nucl. Phys. B **32**, 221 (1971).
38. N.K. Glendenning, *Compact Stars*, 2nd ed. (Springer, Berlin, 2000).
39. G.A. Lalazissis, J. Knig, P. Ring, Phys. Rev. C **55**, 540 (1997).
40. C.J. Horowitz, L. Piekarewicz, Phys. Rev. Lett. **86**, 5647 (2001).
41. B.G. Todd-Ruttel, J. Piekarewicz, Phys. Rev. Lett. **95**, 122501 (2005).
42. S. Typel, H.H. Wolter, Nucl. Phys. A **656**, 331 (1999).
43. E.N.E. van Dalen, C. Fuchs, A. Faessler, Eur. Phys. J. A **31**, 29 (2007).
44. Fabrizio Grill, Constança Providência, Sidney S. Avancini, Phys. Rev. C **85**, 055808 (2012).
45. C. Pethick, A. Potekhin, Phys. Lett. B **427**, 7 (1998).
46. M. Prakash, J.M. Lattimer, J.A. Pons, A.W. Steiner, S. Reddy, Lect. Notes Phys. **578**, 364 (2001).
47. Alan L. Goodman, Nucl. Phys. A **352**, 30 (1981).